ADVANCED FUNCTIONAL MATERIALS
www.afm-journal.de

Highly Deformable Double-Sided Neural Probe with All-in-One Electrode System for Real-Time In Vivo Detection of Dopamine for Parkinson's Disease

Han Hee Jung, Jeongdae Ha, Jeongrak Park, Seongtak Kang, Jinmo Kim, Han Na Jung, Samhwan Kim, Junwoo Yea, Hyeokjun Lee, Saehyuck Oh, Janghwan Jekal, Soojeong Song, Jieun Son, Tae Sang Yu, Youngjeon Lee, Jinyoung Won, Kyung Seob Lim, Yoon Kyeung Lee, Hohyun Keum, Taeyoon Lee, Young Min Song, Jae-Woong Jeong, Jong-Cheol Rah, Ji-Woong Choi, Sheng Xu, Yong-Seok Oh, and Kyung-In Jang**

Precise monitoring of neurotransmitters, such as dopamine (DA), is critical for understanding brain function and treating neurological disorders since dysregulation of DA implicates in a range of disorders, including Parkinson's disease (PD), schizophrenia, and addiction. This study proposes a multi-deformable double-sided (MDD) DA-sensing probe with the three-electrode system in all-in-one form for reliable real-time monitoring of DA dynamics by integrating working, reference, and counter electrodes on a single probe. The proposed probe achieves high DA sensitivity and selectivity in virtue of enzyme immobilization on the 3D nanostructures grown on working electrode. Also, the serpentine design is employed for the electrodes to withstand in various deformations by achieving high stretchability and manage the stress induced on the probe. Experimental and computational analysis demonstrates an effective reduction in induced-stress on the electrodes. The MDD DA-sensing probe is implanted into the brain with success to enable real-time, in vivo monitoring of DA levels in rodents. Furthermore, DA dynamic changes are monitored before and after treatment with L-DOPA in hemi-PD mice. This extremely deformable implantable probe has the potential for use in the study and treatment of neurodegenerative diseases, providing reliable monitoring of DA dynamics with minimal damage to brain tissue.

1. Introduction

As the elderly population increases. The prevalence of neurodegenerative disorders is also increasing.[1–3] Among the neurodegenerative diseases, Parkinson's disease (PD) is one of the most frequent neurological disorders worldwide.[4] The inadequate control of dopamine (DA) levels in the central nervous system (CNS) is associated with the pathogenesis of this prevalent neurological condition, as DA is one of the most important catecholamine neurotransmitters that is widely distributed throughout the CNS.[5] DA regulates several aspects of the brain circuitry, playing an important role in motivation, motor control, memory, reward, and other related functions.[6–9] Therefore, as a powerful neurotransmitter, analyzing DA levels in the brain is critical for studying neurodegenerative disorders, particularly PD.

Real-time monitoring of DA levels in the brain is crucial, and various techniques have been developed to achieve

H. H. Jung, J. Ha, J. Yea, H. Lee, S. Oh, J. Jekal, S. Song, J. Son, T. S. Yu, K.-I. Jang
Department of Robotics and Mechatronics Engineering
Daegu Gyeongbuk Institute of Science and Technology (DGIST)
Daegu 42988, Republic of Korea
E-mail: kijang@dgist.ac.kr

H. H. Jung, J. Park, J. Kim, S. Kim, H. Lee, J.-C. Rah, J.-W. Choi, Y.-S. Oh, K.-I. Jang
Brain Engineering Convergence Research Center
Daegu Gyeongbuk Institute of Science and Technology (DGIST)
Daegu 42988, Republic of Korea
E-mail: ysoh2040@dgist.ac.kr

The ORCID identification number(s) for the author(s) of this article can be found under https://doi.org/10.1002/adfm.202311436

DOI: 10.1002/adfm.202311436

J. Park, Y.-S. Oh
Department of Brain Sciences
Daegu Gyeongbuk Institute of Science and Technology (DGIST)
Daegu 42988, Republic of Korea

S. Kang
Department of Neurology
University of California San Diego
La Jolla, CA 92093, USA

J. Kim, J.-W. Choi, Y.-S. Oh, K.-I. Jang
Department of Electrical Engineering and Computer Science
Daegu Gyeongbuk Institute of Science and Technology (DGIST)
Daegu 42988, Republic of Korea

this, ranging from microdialysis to fast-scan cyclic voltammetry (FSCV) techniques, using different types of neural probes.[10–12] While various types of probes have been proven to be useful tools for studying DA dynamics in the brain, they often suffer from drawbacks associated with the use of rigid materials.[13–15] One of the most significant drawbacks is the potential for undesirable tissue damage caused by the mechanical mismatch between the rigid probe and the soft tissues of the brain.[16–18] This can lead to inflammation and scarring, which can interfere with signal detection due to electrode movement or instability, making it challenging to use the probe for long-term implantation.

To address the issues associated with rigid neural probes, flexible neural probes have been developed, which use thin metal electrodes encapsulated with soft polymers such as polyimide[19,20] or PDMS.[21,22] This approach has demonstrated several advantages, including higher stability and reduced inflammatory responses due to the similarity of the probe's Young's modulus with that of brain tissues, resulting in less tissue damage.[18,22–27] Despite these advances, using a three-electrode system with multiple probes, such as the working electrode (WE), reference electrode (RE), and counter electrode (CE), still requires drilling two or more holes in the skull, making minimally invasive implantation of flexible neural probes challenging while maintaining the three-electrode system for accurate real-time monitoring of DA dynamics in the brain.[28–31]

Our study proposes an innovative solution to the limitations of conventional rigid neural probes. Our highly stretchable, double-sided, all-in-one structure incorporates a three-electrode system in a single probe, which allows for real-time measurement of DA dynamics in the brain. By utilizing this system, we are able to monitor reliable signals from the brain while reducing tissue damage and improving signal detection through electrode stability. Our design offers a larger electrode area than single-sided design without increasing the lateral size by embedding the WE and RE on the single side of the substrate, allowing for precise sensing by keeping the distance sufficiently small between WE and RE.[32,33] The CE is strategically positioned on the other side, which enhances the signal-to-noise ratio by increasing the surface area. Conventional flexible neural probes typically position their thin metal electrodes at the neutral plane to minimize stress-induced damage caused by deformation. However, the proposed multi-deformable double-sided (MDD) DA-sensing probes have their three electrodes located further away from the neutral plane, which inherently makes them mechanically unstable due to their unique double-sided design. Such structural characteristics can render them susceptible to stress-induced damage from deformation. To overcome this issue, we have adopted a serpentine patterned electrode design, which improves mechanical stability under various deformations. To the best of our knowledge, no prior work has proposed a double-sided, all-in-one probe with a three-electrode system in a serpentine pattern design. Furthermore, in vivo experiments on wild-type rats and hemi-PD mice have confirmed the sensitivity and reliability of our double-sided neural probe. Our study demonstrates the significant advantages of our novel design, which offers unprecedented levels of precision, stability, and sensitivity in neural recording technology.

2. Results and Discussion

2.1. Multi-Deformable Double-Sided DA-Sensing Probe Design

Figure 1a is an exploded schematic view of the MDD DA-sensing probe to illustrate the layer information and associated components. The MDD DA-sensing probe comprises three main components, which include a top component, a bottom component, and a stretchable poly(dimethylsiloxane) (PDMS; ≈250 μm in thickness) substrate to integrate micrometer-scale three electrodes (WE, RE, and CE) in a single probe to perform a reliable electrochemical analysis. The top component is integrated with a bi-layer of Cr/Au (7 nm/200 nm in thickness) for WE (r = 135 μm) and RE (100 × 700 μm^2) in serpentine design on a dielectric polymer layer (≈5 μm in thickness). The Zinc Oxide (ZnO) seed layer

H. N. Jung
Department of Applied Bioengineering
Graduate School of Convergence Science and Technology
Seoul National University
Seoul 08826, Republic of Korea
Y. Lee, J. Won
National Primate Research Center
Korea Research Institute of Bioscience and Biotechnology (KRIBB)
Daejeon 28116, Republic of Korea
K. S. Lim
Futuristic Animal Resource and Research Center
Korea Research Institute of Bioscience and Biotechnology (KRIBB)
Daejeon 28116, Republic of Korea
Y. K. Lee
Division of Advanced Materials Engineering
Jeonbuk National University
Jeonju, Jeonbuk 54896, Republic of Korea
H. Keum
Digital Health Care R&D Department
Korea Institute of Industrial Technology
Cheonan, Chungnam 31056, Republic of Korea
T. Lee
School of Electrical and Electronic Engineering
Yonsei University
Seoul 03722, Republic of Korea
Y. M. Song
School of Electrical Engineering and Computer Science
Gwangju Institute of Science and Technology
Gwangju 61005, Republic of Korea
J.-W. Jeong
School of Electrical Engineering
Korea Advanced Institute of Science and Technology
Daejeon 34141, Republic of Korea
J.-C. Rah, J.-W. Choi, Y.-S. Oh, K.-I. Jang
Korea Brain Research Institute
Daegu 41062, Republic of Korea
S. Xu
Department of Nanoengineering
University of California San Diego
La Jolla, CA 92093, USA
K.-I. Jang
Artificial Intelligence Major in Department of Interdisciplinary Studies
Daegu Gyeongbuk Institute of Science and Technology (DGIST)
Daegu 42988, Republic of Korea
K.-I. Jang
Institute of Next-generation Semiconductor Convergence Technology
Daegu Gyeongbuk Institute of Science and Technology (DGIST)
Daegu 42988, Republic of Korea
K.-I. Jang
ENSIDE Corporation
Daegu 42988, Republic of Korea

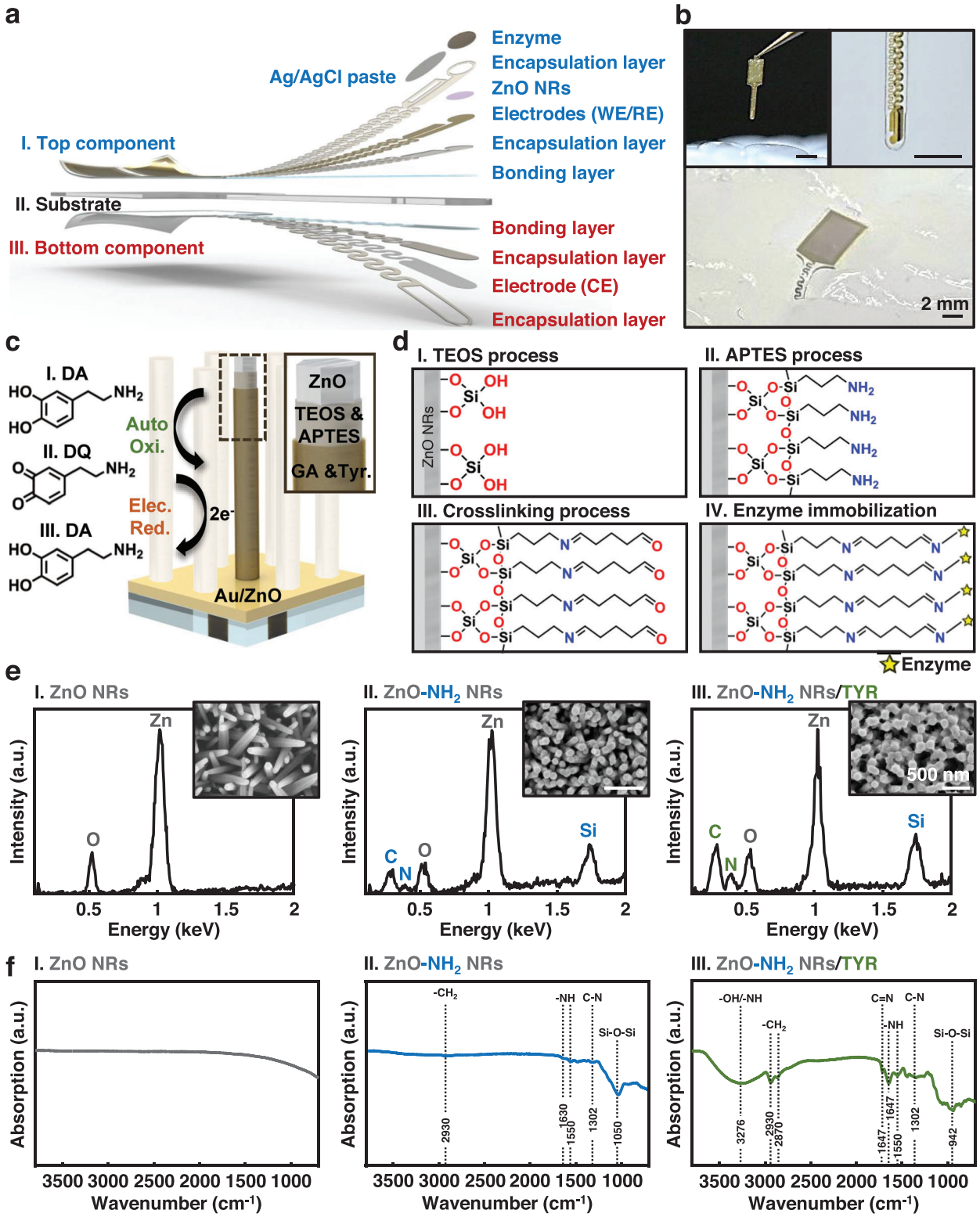

Figure 1. a) Exploded-view schematic diagram illustrating the MDD neural probe architecture; b) Optical images of magnified view of the MDD neural probe in a phantom brain (0.6% agarose gel); The insets show an enlarged overall view of the fabricated MDD neural probe and a magnified view of the three electrodes (WE, RE, and CE) integrated on a single neural probe; c) Schematic illustration of the enzyme (TYR) immobilized onto ZnO NRs in which is hydrothermally grown on the WE surface (Cr/Au/ZnO; Thickness: 7 nm/200 nm/25 nm) and electrochemical principle of the MDD neural probe responsive to DA through immobilized enzyme; d) Schematic illustration of depicting enzyme immobilization process with its corresponding chemical structures on the WE of the MDD neural probe; e) EDX analysis and f) FTIR spectra during enzyme immobilization processes to confirm ZnO NRs (I), amine-functionalized ZnO NRs (ZnO—NH_2 NRs; II), and TYR immobilization (III).

is positioned on the WE surface to cultivate ZnO nanorods (NRs) for enhanced sensitivity to DA due to the increased surface area, which is closely related to the sensitivity of electrochemical detection. The enzyme (tyrosinase, TYR) is anchored to the hydrothermally grown ZnO NRs through several steps of surface treatment to achieve robust immobilization on the WE electrode surface. For the stable and reproducible electrical potential during DA detection, the Ag/AgCl paste (≈100 µm in thickness) is screen printed onto the RE. On the other hand, the bottom component comprises a Ti/Pt bi-layer with thickness of 20 and 100 nm, serving as the counter electrode for the MDD DA-sensing probe. This material (Pt) is renowned for its widespread application as a CE and is configured in a serpentine pattern.[34] The CE measures 0.038×0.115 cm^2 and is enveloped by a dielectric polymer layer ≈5 µm thick. These top and bottom components are integrated on both sides of the PDMS substrate, allowing for the utilization of the probe as an all-in-one device featuring a three-electrode system. This configuration incorporates the WE, RE, and CE into a single probe. Additional details regarding the fabrication process can be found in the Experimental Section and Supporting Information. Figure 1b shows an overall representative image of the fabricated MDD neural probe (upper left inset), a microscopic image of MDD DA-sensing probe tip with WE/RE on one side of the probe and the other side with CE (upper right inset), and optical image of the MDD DA-sensing probe implanted on a phantom brain, showing minimal invasive insertion (bottom).

2.2. Immobilization of Enzyme on to the Hydrothermally Grown ZnO NRs

Figure 1c shows the schematics of the MDD DA-sensing probe's WE surface with immobilized enzyme (TYR) on the hydrothermally grown ZnO nanorods (NRs) with the reaction scheme for DA detection. The detection mechanism of DA is based on the oxidation of DA into *o*-dopaquinone (DQ) (Equation (1)), and the subsequent electrochemical reduction of DQ on the surface of WE at low potential (Equation (2)).[35]

$$\text{Dopamine} + 1/2O_2 \xrightarrow{\text{TYR}} o - \text{Dopaquinone} + H_2O \quad (1)$$

$$o - \text{Dopaquinone} + 2H^+ + 2e^- \text{ Dopamine} + H_2O \quad (2)$$

The immobilization of enzyme (TYR) is the crucial step in the fabrication process of the MDD DA-sensing probe for the selective detection of DA. For the effective immobilization of TYR on WE with a larger surface area to increase the reduction current for higher sensitivity, the 3D nano-forest-like structures are utilized by hydrothermally grown ZnO NRs on the WE surface of the MDD DA-sensing probe. The development of ZnO NRs is well explained in the experimental section.

To immobilize the enzyme on the WE of the probe, the hydrothermally grown ZnO NRs (Figure 1d-I) are coated with silica to form ZnO—O—Si, which hydrolyzed tetraethyl orthosilicate (TEOS, precursor of silica) condensed on the surface of ZnO NRs.[36] After the silanization process, 3-(Aminopropyl) triethoxysilane (APTES, amino-modification reagent) is added to the reaction solution to form amine-functionalized ZnO NRs (ZnO—NH_2 NRs) by sol-gel process (Figure 1d-II). After amine-functionalization of ZnO NRs, the TYR is immobilized on the ZnO—NH_2 NRs structures by cross-linking (CL) with glutaraldehyde (GA), which acts as a bridge with aldehyde group between primary amino groups (—NH_2) of silanized ZnO NRS and the terminal amino groups of the TYR (Figure 1d-III,IV).[37] The processes involved in enzyme immobilization were characterized with energy dispersive X-ray (EDX) analysis and scanning electron microscopy (SEM), as illustrated in Figure 1e. In Figure 1e-I, the EDX spectrum offers confirmation of the presence of well-developed ZnO NRs, as evidenced by the prominent intensity peaks corresponding to oxygen (O) and zinc (Zn). Additionally, the SEM images reveal densely populated ZnO NRs, assuming a hexagonal pillar-like morphology, as clearly depicted in the inset of Figure 1e-I. Upon subjecting the ZnO NRs to the amine-functionalization process, the EDX analysis reveals additional intensity peaks associated with silicon (Si), nitrogen (N), and carbon (C) (Figure 1e-II). These peaks signify interactions with TEOS and APTES, corresponding to the processes of silanization and amine-functionalization, respectively. The SEM image portrays ZnO—NH_2 NRs with a modified surface, appearing rounder and thicker in comparison to ZnO NRs. The investigation of the TYR immobilization process, represented in Figure 1e-III, indicates a significant enhancement in the intensity of N, C, and O peaks in comparison to the preceding amine-functionalization step (Table S2, Supporting Information). The SEM image inset of Figure 1e-III. further elucidates the observation of ZnO—NH_2 NRs with TYR entities interlinked. Moreover, the elemental composition analysis by EDX (Table S1 and Figure S1, Supporting Information)

Additionally, Fourier transform infrared spectroscopy (FTIR) was used to confirm the successful immobilization of enzyme (Figure 1f; Figure S2, Supporting Information). As shown in Figure 1f-I, the spectrum of ZnO NRs showed no significant peaks. However, the presence of critical peaks was evident in the spectra of ZnO—NH_2 NRs after TEOS and APTES process (Figure 1f-II). Specifically, the spectra displayed an asymmetric vibration peak at 1050 cm^{-1}, attribute to the silanization formed on ZnO NRs.[38–40] Furthermore, characteristics absorption peaks associated with —CH_2 (2930 cm^{-1}), N—H (1550 cm^{-1}, 1630 cm^{-1}), and C—N (1302 cm^{-1}) were identified.[41–43] These findings provide compelling evidence for the proposed amine-functionalization process.

The FTIR spectra of the TYR-immobilized surface on the working electrode (WE) exhibited noteworthy features. Notably, a broad peak, centered at 3276 cm^{-1}, is observed, which can be attributed to the stretching vibrations of N—H and O—H in the enzyme.[43] Additionally, a distinct absorption peak at 1647 cm^{-1}, corresponding to C═N,[41,42] is evident in the spectra. Moreover, there is a noticeable increase in the intensity of peaks associated with C—N (1302 cm^{-1}), N—H (1550 cm^{-1}, 1647 cm^{-1}), and —CH_2 (2930 cm^{-1}). These observations, based on the FTIR spectra, provide compelling evidence for the successful immobilization of TYR on the WE of the MDD DA-sensing probe.

2.3. Electrochemical Characteristics of MDD DA-Sensing Probe

The electrochemical properties for each surface modification process are investigated by the cyclic voltammetry (CV) method to

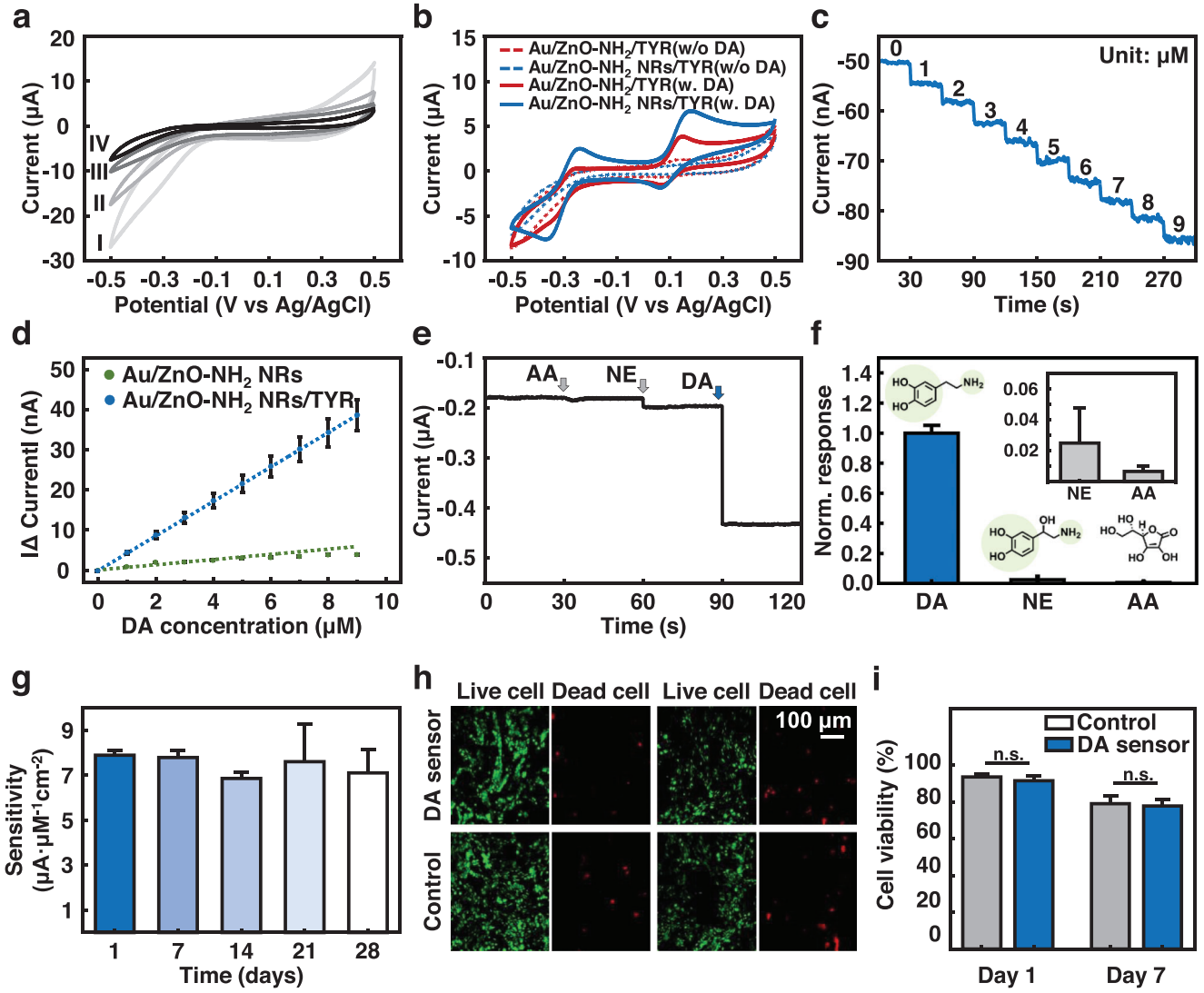

Figure 2. a) Cyclic voltammetry of (I) Au, (II) Au/ZnO seed layer, (III) Au/ZnO NRs, and (IV) Au/ZnO NRs/CL/TYR in 0.05 M PBS solution (pH 7.4) at a scan rate of 150 mV s^{-1}; b) Cyclic voltammetry of the enzyme modified electrode based on Au/ZnO/TYR and Au/ZnO NRs/CL/TYR in 0.05 M PBS (pH 7.4) with and without 100 μM DA at a scan rate of 150 mV s^{-1}; c) Amperometric response of the MDD DA-sensing probe on the successive addition of 1 μM DA over time in 0.05 M PBS (pH 7.4) at −350 mV versus Ag/AgCl; d) The calibration curves for Au/ZnO NRs modified electrodes with immobilized enzyme (blue) and without the enzyme (green); e) Temporal continuous electrochemical behaviors and f) normalized responses indicating high selectivity of the MDD DA-sensing probe to 50 μM DA when present with various neurotransmitters such as 500 μM AA, and 50 μM NE; g) Long-term stability test with measured sensitivity of the MDD DA-sensing probe when immersed in 0.05 M PBS (pH 7.4, 30 °C) for 4 weeks; h) Fluorescence images of live (green) and dead (red) SH-SY5Y cells cultivated on the MDD DA-sensing probe for 1 day and 7 days; i) Bar graph displaying the viability at day 1 and 7 of the SH-SY5Y cells cultured on the MDD DA-sensing probe (n = 3 samples).

compare the bare Au, Au/ZnO seed layer, Au/ZnO NRs, and Au/ZnO—NH_2 NRs/TYR electrodes, as shown in **Figure 2**a. The CV curve of the bare Au electrode (curve I) shows the largest current response compared to the CV curves of other modified electrodes, such as Au/ZnO seed layer (curve II) (ZnO; ≈7.261×10^7 cm^{-1} Ω^{-1} in conductivity),[44] Au/ZnO NRs (curve III), and Au/ZnO—NH_2 NRs/TYR (curve IV), owing to the excellent electrical conductivity of Au (≈0.452×10^6 cm^{-1} Ω^{-1}). The current response of CV starts to decrease as the electrode modification process advances, due to the reduction of electrical conductivity. Furthermore, the CV results corroborate the increased surface area of WE attributed to the presence of ZnO NRs (curve III), as evidenced by a reduced current response in comparison to the electrode featuring solely the ZnO seed layer (curve II). The redox current of the enzyme immobilized electrode (TYR, curve IV) on ZnO NRs significantly decreased due to the limited conductivity, indicating the successful immobilization of the enzyme onto the WE of the MDD DA-sensing probe.

In this regard, electrochemical stability assessments were performed during the enzyme immobilization process on four distinct electrode configurations: Au; Au/ZnO; Au/ZnO NRs; Au/ZnO—NH_2 NRs/TYR. These measurements were conducted at room temperature, employing a scan rate of 150 mV s^{-1} in a 100 μM DA solution, encompassing 50 consecutive

oxidation–reduction cycles. The quantification of electrochemical activity was expressed as the percentage loss of electrochemical activity (LEA; in %) (Equation (3)):[45–47]

$$\mathrm{LEA} = \frac{\Delta Q}{Q_2} * 100 = \frac{Q_2 - Q_\#}{Q_2} \quad (3)$$

where ΔQ denotes the difference between the oxidation charge (in C) of the second cycle (Q_2) and the specific oxidation–reduction cycle under assessment ($Q_\#$). As depicted in Figure S3 (Supporting Information), in the case of the WE comprising Au/ZnO, a notable reduction in electrochemical activity becomes evident with an increasing number of oxidation–reduction cycles. This results in a notable escalation of the LEA, peaking at 47.8% after 50 consecutive cycles. In contrast, the LEA for Au, Au/ZnO NRs, and Au/ZnO—NH_2 NRs/TYR exhibit a slight decline in electrochemical activity, stabilizing at 16.4%, 18.6%, and 10.6%, respectively. Consequently, it can be deduced that Au/ZnO—NH_2 NRs/TYR showcases commendable electrochemical stability when exposed to DA.

A comparative assessment of the electrochemical characteristics of the constructed MDD DA-sensing probe, both with and without ZnO NRS, is conducted in the absence and presence of DA, as depicted in Figure 2b. The redox peak of the electrode with ZnO NRs in the absence of DA barely shows any obvious current peak. However, when the CV is measured in the presence of DA, the electrode with ZnO NRs shows the largest current response compared to that of the electrode with ZnO, and a notable reduction peak (peak potential of −330 mV) is observed due to the electrocatalytic reduction of DA. The enhanced current response can be attributed to the high aspect ratio of ZnO NRs, which provide a high specific area for enough enzyme loading on the ZnO NRs.

Amperometric response of the fabricated MDD DA-sensing probe is conducted to determine the performance in DA-sensing. This involves the sequential addition of DA within a concentration range of 1–9 μM, as shown in Figure 2c. The MDD DA-sensing probe exhibited excellent amperometric response, demonstrating rapid detection capabilities with a short response time of ≈1 s, specifically upon the successive addition of 1 μM DA. To highlight the significance of the enzyme (tyrosinase) in DA sensing, evaluations were conducted on the reactivity of the WE within the developed DA-sensing probe under both enzyme-immobilized and enzyme-absent conditions. As depicted in Figure 2d, a comparative analysis of the Au/ZnO NRs modified with and without the enzyme revealed that the DA-sensing probe lacking TYR exhibited minimal responses to DA, indicating a sensitivity of 0.65 nA μM^{-1} (R^2 = 0.8734) and a limit of detection (LOD) of ≈320 nM. In contrast, the TYR-immobilized DA-sensing probe demonstrated a significantly enhanced sensitivity of 4.299 nA μM^{-1} (R^2 = 0.999) with LOD of ≈150 nM. Additionally, the cyclic voltammetry test confirmed that the presence of TYR resulted in higher current intensity responses to DA, underscoring the pivotal role played by TYR in augmenting the DA sensing capabilities of the probe (Figure S4, Supporting Information).

The anti-interference properties are critical parameters for electrochemical sensing, as the working potential may be related to the reduction of other potential interfering species present with DA among other biochemical analytes, including ascorbic acid (AA) and norepinephrine (NE), whose reduction potential and molecular structures are similar to that of DA, respectively. Also, better selectivity will ensure high accuracy during measurement. As shown in Figure 2e, the temporal measurements of amperometric responses were assessed by successive addition of 50 μM DA, 500 μM AA, and 50 μM NE. Adding DA resulted in a significant and rapid current response, whereas adding interfering species (500 μM AA and 50 μM NE) caused negligible current variations. Normalized current response for DA detection with other interfering species was illustrated by the histogram in Figure 2f. When the amperometric response of 50 μM DA was set as 100%, the graph shows that the interfering species caused a very low response, i.e., for 50 μM NE (≈2.5%), and for 500 μM AA (≈0.7%). The inset of Figure 2f presents the current response for interfering species addition of AA and NE. The long-term stability of the MDD DA-sensing probe was also evaluated, and the associated histogram in Figure 2g shows that it retained ≈90% of its initial sensitivity over a four-week period, demonstrating good stability in both performance and material terms for the MDD DA-sensing probe (Table S2 and Figure S5, Supporting Information). To assess the biocompatibility of the MDD DA-sensing probe, representative confocal fluorescence images from cultured catecholaminergic cells (SH-SY5Y cells)[48] on the MDD DA-sensing probe showed a statistically negligible difference in cell viability when compared with control up to 7 days (Figure 2h–I).

2.4. Computational Stress Analysis of the MDD DA-Sensing Probe in Complex Deformation

The electrode configuration of the MDD DA-sensing probe is inherently vulnerable to mechanical strain due to the positioning of double-sided electrodes further from the neutral plane located in the substrate, resulting in potential mechanical failure. To overcome this limitation, electrodes are engineered with a serpentine pattern to minimize mechanical strain induced by various deformations, including simple (stretching, bending) and complex (buckling, torsion, rolling) deformations. Finite element analysis (FEA) was employed to verify the effectiveness of this design in reducing mechanical strain on the electrodes. A comparative stress analysis was conducted on all electrodes (WE, RE, CE) with both serpentine-lined (SPL) and straight-lined (STL) design. The resulting stress was normalized to the ultimate strength of each bulk material (140 MPa for CE and 100 MPa for WE and RE) in order to intuitively evaluate the mechanical stability of each electrode. The strength of a metal is influenced by its thickness, and there is a tendency for strength to increase as the thickness decreases. However, not only thickness but also various other parameters (such as grain size, and morphology) can also affect the strength. [49,50] Therefore, to achieve a more intuitive stress normalization, the strength of the bulk metal was used.

With a 30 μm stretching in the x-direction, the average stress for the top electrodes (WE/RE) and bottom electrode (CE) of the STL were 302 and 785 MPa, respectively. In contrast, the SPL electrodes exhibited significantly lower average stress, with readings of 25.9 and 39.7 MPa for the WE/RE and CE electrodes, respectively (Figure S6a, Supporting Information). These results demonstrate a substantial reduction in stress when comparing SPL to STL electrodes. This suggests that SPL electrodes

maintain their mechanical stability even under an elongation of up to 50 μm, whereas the STL electrodes can experience plastic deformation and even rupture at elongations as low as a few micrometers. When bent in the y- and z-directions, the stress of the electrodes exhibited a similar pattern to that observed during stretching (Figure S6b,c, Supporting Information). Specifically, the average stress of the STL electrodes was ≈9 folds higher than those of the SPL electrodes for bending in the y- and z-directions, respectively. **Figure 3**a–c illustrates the average stress experienced by both the STL and SPL electrodes during complex deformations, such as buckling (Figure 3a), torsion (Figure 3b), and rolling (Figure 3c). The results exhibit similar tendencies to those obtained during simple deformations. Notably, the buckling, occurring while inserting the probe into the brain, stress revealed significant differences in the average stress of the STL and SPL electrodes. As shown in Figure 3a, the SPL electrodes remained intact even when compressed up to 3 mm, whereas the STL electrodes suffered damage when the probe was buckled under a compression of ≈100 μm. Furthermore, the stress analysis on the probe under torsional deformations demonstrates the outstanding mechanical stability of the SPL. When the probe is rolled (2π rad) as shown in the Figure 3b, the average stress of the STL electrodes (WE/RE ≈207 MPa, CE ≈649 MPa) is much higher than the SPL electrodes (WE/RE ≈112 MPa, CE ≈166 MPa). In this rotation state, when a compressive force is added to the probe, rolling deformation is induced, and the average stress of the SPL electrodes (WE/RE ≈54 MPa, CE ≈113 MPa) shows a significantly lower value than that of STL electrodes (WE/RE ≈432 MPa, CE ≈695 MPa) (Figure 3c). All of the aforementioned stress analysis results demonstrate that the SPL electrodes are mechanically stable compared to the STL electrodes. Despite the configuration of the proposed probe inherently having structural instability, the design of SPL electrodes ensures the reliability of the probe even during undesired deformation in virtue of serpentine design for the electrodes. Figure 3d–f displays optical micrographs and their corresponding SEM images of the MDD DA-sensing probe which is capable of withstanding various deformation modes such as buckling (Figure 3d), torsion (Figure 3e), and rolling (Figure 3f). The double-sided integration structure that facilitates the three-electrode system for the MDD DA-sensing probe ensures mechanical robustness and reliable electrical functionality of the three electrodes (WE, RE, and CE) during dynamic deformations.

PDMS is often subjected to hygroscopic swelling strain in solvents, such as bio-fluid.[51,52] Therefore, the electrodes experience strain (≈0.02%) due to PDMS swelling. However, the relatively low modulus of PDMS (≈600 kPa) results in negligible strain on the electrodes, and consequently, the mechanical instability caused by water absorption in an in-vivo state is almost nonexistent (Figure S7, Supporting Information).

2.5. In Vivo, Real-Time Monitoring of the Striatal DA Dynamics in Normal Mice Model

For in vivo, real-time monitoring of the striatal DA dynamics with electrical stimulation (**Figure 4**a–c), the MDD DA-sensing probe and the electrical stimulation electrode are implanted in the striatum (Str) and the medial forebrain bundle, respectively (Figure 4b; Figure S12a, Supplementary Information). As illustrated in Figure 4b, the MFB of the nigrostriatal pathway links the substantia nigra pars compacta (SNpc) and the caudate putamen (CPu) of the Str. The DA signal in the Str was gradually increased during the electrical MFB stimulation (Figure 4c), whereas the DA signal was restored to the normal level after cessation of electrical stimulation, likely due to the homeostatic recovery.[53] In contrast, without electrical stimulation applied to the MFB, we didn't observe any significant change in the DA signal (≈−46 nA). The DA dynamics after electrical MFB stimulation were consistent in all animals tested (n = 4). The average current change was measured at ≈2.8 nA with MFB stimulation but remained baseline without electrical stimulation (Figure S8, Supporting Information).

Moreover, we tested the biocompatibility of the MDD DA-sensing probe with chronic implantation in the brain. Using immunohistological analysis of reactive glial markers, we assessed neuroinflammatory responses to chronic implantation of the DA-sensing probe. Astrocytic deposition and microglial activation were monitored with immunostaining of an astrocyte marker Gfap and reactive microglia marker Iba1, respectively. No observation shown in any significant difference in neuroglial inflammatory responses between the DA probe-implanted group (w. implantation) and the sham-operated group (w/o implantation) (Figure S9, Supporting Information). Collectively, these data demonstrated the functionality of the MDD DA-sensing probe to monitor DA dynamics in vivo, as well as its biocompatibility with brain implantation.

2.6. Real-Time Measurement of Pharmacological DA Dynamics in the Parkinson's Disease (PD) Mice Model

Next, we applied the MDD DA-sending probe to monitor the DA dynamics in pathological in vivo mode in which the DA level was depleted and further replenished with pharmacological treatment. To this end, we adopted a hemi-parkinsonian (hemi-PD) mouse model in which dopaminergic neurons are degenerated only in the lesioned hemisphere (Figure 4d).[54] With this hemi-PD model, we could easily monitor the dynamic changes in DA level before and after pharmacological treatment of L-DOPA a DA precursor because of its DA-depletion status. To generate the hemi-PD model, we injected 6-OHDA, a dopaminergic neuron toxin into the unilateral MFB prior to behavioral and histological validation 2 weeks post-surgery. In the locomotive behavior test, the hemi-PD model mice displayed ipsiversive rotation toward the lesioned hemisphere. But after apomorphine (APO) injection, their rotational behaviors were dramatically switched from ipsiversive to contraversive direction (Figure 4e,f). After the behavior test, all the mice were sacrificed and perfused for histological validation of unilateral degeneration of dopaminergic neurons. STR and SNpc regions were immunostained for tyrosine hydroxylase (TH) a dopaminergic neuronal marker and dopamine transporter (DAT) a dopaminergic axon terminus marker. As compared to the intact hemisphere (left), the 6-OHDA lesioned side (right) showed complete loss of TH and DAT in the Str and also TH in the SNpc, suggesting unilateral degeneration of dopaminergic axons at the CPu and their somas at the SNpc (Figure 4g; Figure S10, Supporting Information).

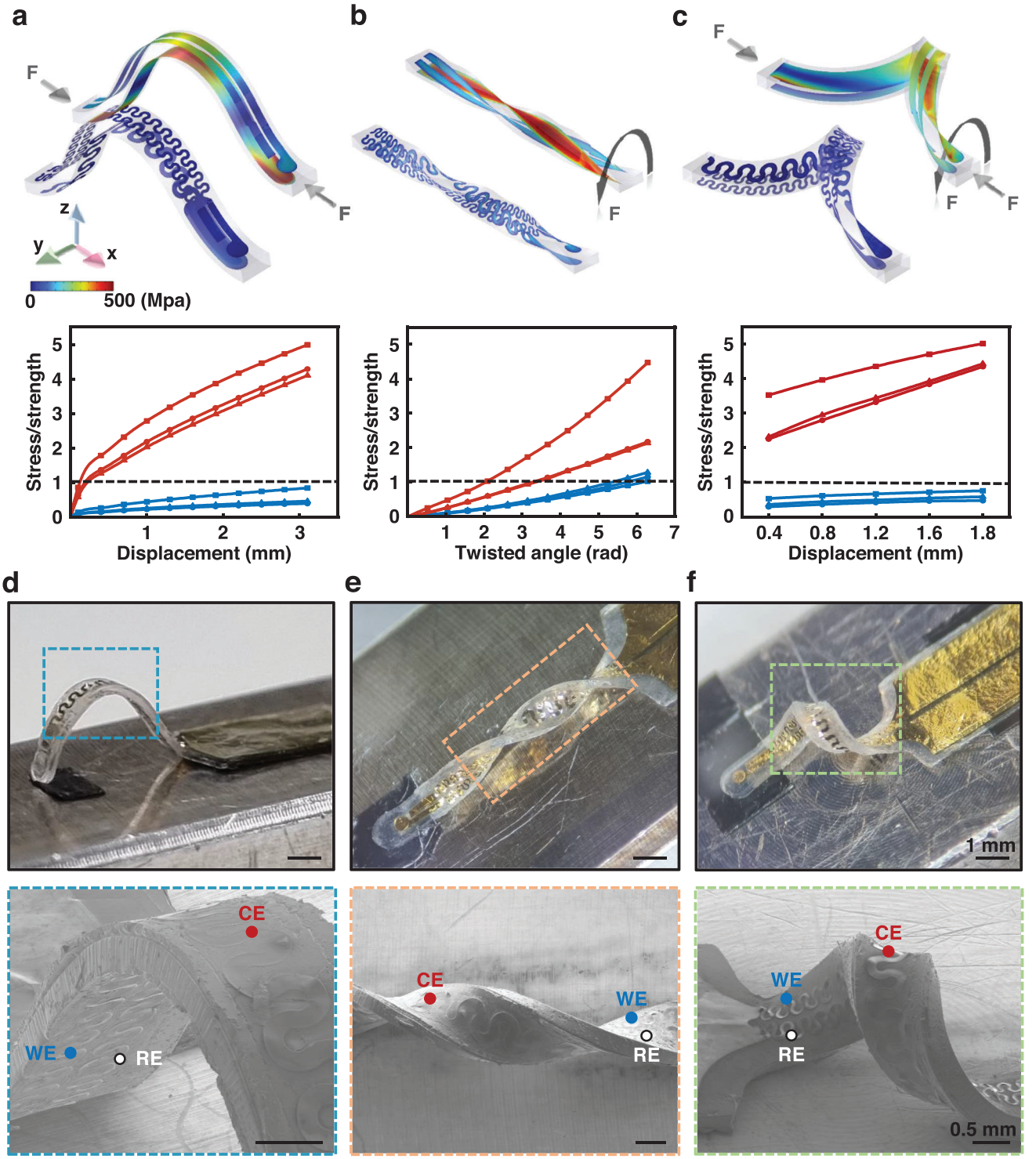

Figure 3. Stress simulation results for MDD DA-sensing probe with electrodes patterned with straight-line (STL) and serpentine-line (SPL), and normalized stress graphs of the MDD DA-sensing probe integrated with three electrodes (WE, RE, and CE) designed as STL (red) and SPL (blue) according to the corresponding deformation: a) buckling, b) twisting and c) rolling. Optical and SEM images of the mechanically deformed MDD DA-sensing probe with extreme deformation: d) buckling; e) twisting; f) rolling.

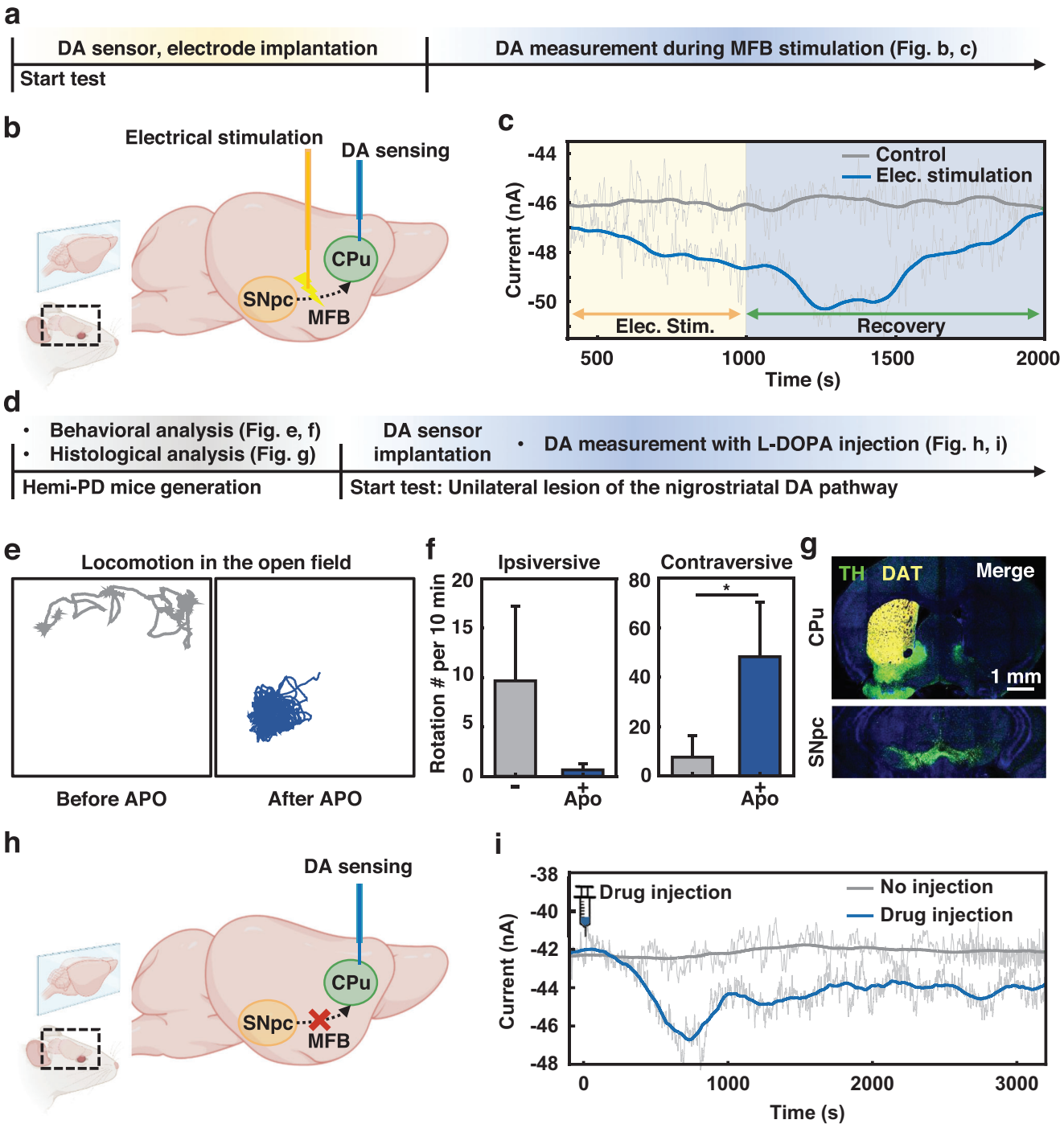

Figure 4. a) Experimental procedure of DA measurement of with electrical stimulation of dopaminergic axon fibers in the MFB of wild-type rat model; b) Schematic illustration of the nigrostriatal dopaminergic pathway in the brain, and the anatomical locations of MDD DA-sensing probe for striatal DA measurement with electrical MFB stimulation; c) In vivo amperometric responses of the DA-sensing probe during electrical MFB stimulation (yellow area) and homeostatic recovery (blue area); d) Experimental schematics on validations of hemi-PD mice model generation, and real-time in vivo assessment to measure the pharmacological conversion of L-DOPA to DA in hemi-PD model mice; e) Representative tracking data for hemi-PD mice model's locomotion before and after APO injection; f) Quantitative analysis of rotational directions (ipsiversive vs contraversive) of hemi-PD mice model before and after APO injection in 10 min; g) Histological validation of unilateral dopaminergic denervation of the hemi-PD mice model. TH (green) and DAT (yellow) as histological markers for dopaminergic axon fibers in the striatum; h) Experimental illustration representing implantation of MDD DA-sensing probe positioned at the CPu region in which dopaminergic axons from SNpc are degenerated; i) In vivo amperometric responses to represent relative DA synthesis from its precursor L-DOPA in the striatum of hemi-PD model.

After this behavioral and histological validation, we applied this hemi-PD mice model to further validate the functionality of the MDD DA-sensing probe during the pharmacological synthesis of DA from its precursor L-DOPA. The MDD DA-sensing probe was implanted into the lesioned Str in the hemi-PD mice model under anesthesia status (Figure 4h). Interestingly, the DA signal in the MDD DA-sensing probe was gradually increased after L-DOPA injection, as compared to no injection control. About 10 min post-injection, the DA level was saturated to the highest level and sustained as long as about an hour (Figure 4i). Collectively, these data demonstrated that the MDD DA-sensing probe is compatible with real-time measurement of pharmacological DA dynamics in the Parkinson's disease (PD) mice model.

3. Conclusion

Recent advancements in neural probe technology have resulted in practical tools for reliable monitoring of neurotransmitters in the brain, by integrating the physical and functional characteristics of neural probe technology. However, challenges related to minimally invasive insertion persist, primarily due to the undesired damage to brain tissue caused by rigid materials and the use of multiple probes, such as WE, RE, and/or CE for a two- or three-electrode system. To address these challenges, we propose a set of ideas, materials, and designs for building a compelling architecture of a highly stretchable double-sided, all-in-one structure that incorporates a three-electrode system, enabling minimally invasive insertion, and allowing for reliable in vivo electrochemical analysis for long-term measurement of DA dynamics in real-time. Effective enzyme immobilization on the 3D nanoforest-like structures grown on the surface of the WE maximized the surface area resulting in high DA sensitivity with an average sensitivity of −4.299 nA μM and a LOD of 150 nM. Furthermore, conventional flexible neural probes position its thin metal electrodes at the neutral plane of the probe to minimize stress-induced damage caused by deformation. The proposed MDD DA-sensing probes have its three-electrodes located further away from the neutral plane, making it susceptible to stress-induced damage from deformation. Therefore, we utilized the serpentine-designed electrodes to overcome this inherent structural vulnerability, which successfully mitigates the structural drawbacks by reducing the induced stress on the electrodes. Additionally, the computational analyses clearly indicate that the implementation of the serpentine design on the electrodes reduces the induced stress on the electrodes by maximum 20-fold compared to that of straight-lined electrodes, from simple stretching and bending to complex buckling, twisting, and rolling, showing the mechanical stability of the MDD DA-sensing probe. We demonstrated the feasibility of in vivo real-time DA level monitoring in wild-type rats and hemi-PD mice. The response of the MDD DA-sensing probe to the induced DA production in the wild-type rat brain indicates that the fabricated probe operates effectively and has reasonable specificity for DA in an in vivo environment. To further assess the feasibility of the MDD DA-sensing probe in the context of pharmacological treatment for PD, we employed a hemi-PD mouse model and validated its effectiveness through behavior and histological analysis. By utilizing this model, we were able to readily monitor the dynamic changes in dopamine levels before and after treatment with L-DOPA. These results demonstrate that the materials and proposed design of the MDD DA-sensing probe have great potential for use as an implantable probe for real-time in vivo monitoring of dopamine with minimal invasiveness and without causing undesired damage to the brain. We believe this proposed study could lead to significant implications for the study of neurological disorders, as it provided researchers with a useful tool for measuring and analyzing dopamine levels in real-time, which can help to better understand the underlying mechanisms of these conditions and potentially lead to the development of more effective treatments for PD as well as other neurological disorders.

4. Experimental Section

Reagents: DI were purchased from Daejung Chemicals & Materials Co. Ltd (Korea). Ethanol were purchased from ChemiTop (Korea). SU-8 were purchased from Kayaku Advanced Materials (MA, USA). Polydimethylsiloxane (PDMS, Sylgard 184) were obtained from Dow Corning, USA). Poly(methyl methacrylate) (PMMA) were purchased from Microchem (USA). Water-soluble tape (Water-Soluble Wave Solder 5414) and Ag/AgCl paste were purchased from 3 M (USA) and Sun Chemical (USA), respectively. SH-SY5Y neuroblastoma cells (CRL-2266) were purchased from ATCC (USA). Hexamethylenetetramine (HMTA) and aqueous ammonia were purchased from Samchun (Korea). Zinc nitrate hexahydrate, tetraethoxysilane (TEOS), 3-aminopropyltriethoxysilane (APTES), glutaraldehyde (GA; 25% water solution), phosphate buffer saline (PBS), potassium phosphate dibasic solution, potassium phosphate monobasic solution, Tyrosinase (TYR; EC 1.14.18.1 2840 U mg^{-1}, from mushroom), dopamine hydrochloride, ascorbic acid (AA), norepinephrine (NE), levodopa (L-DOPA) were purchased from Sigma–Aldrich (USA) and used as received.

Preparation of the Substrate Layer for MDD DA-Sensing Probe: Spin-casting photocurable epoxy (SU-8 2100) to develop molds for substrate layer. Spin-casting the PDMS onto the developed mold. Taking-off the substrate layer for the MDD DA-sensing probe with a tweezer carefully. SU-8 2100 (Kayaku Advanced Materials, USA) was applied through spin casting and thermally cured on a 4-inch silicon wafer to establish the mold for crafting the substrate layer of the MDD DA-sensing probe. Photolithographic techniques were employed to define the mold according to the desired design. Subsequently, PMMA (MicrChem, USA) was spin cast atop the mold pattern to serve as an anti-adhesion layer, facilitating the later removal of the PDMS. PDMS (1:10 ratio) was poured into the patterned mold, and excess PDMS was meticulously eliminated. The PDMS-filled mold was then subjected to curing in an oven at 60 °C for an adequate duration, ≈30 min, to achieve PDMS solidification. Post-curing, the patterned PDMS substrate layer was carefully extracted from the mold employing tweezers (Figure S11, Supporting Information).

Fabrication of Top Component (We/Re) of the MDD DA-Sensing Probe: Spin-casting PMMA (≈1 μm in thickness) formed a thin sacrificial layer on a glass substrate ($55 \times 72 \times 1$ mm^3) to facilitate release. Spin-casting and performing photolithography of a photocurable epoxy (SU-8 2005) yielded an overcoat on the PMMA, depositing thin layers of metal by electron beam evaporation (Cr/Au; 7 nm/200 nm in thickness), performing photolithography, wet-etching to create the WE and RE of MDD DA-sensing probe. Depositing thin layers of ZnO (25 nm in thickness) and yielding on the WE surface as a seed layer by RF sputtering and lift-off-techniques. Spin-casting and photolithography of another layer of a photocurable epoxy, followed by spin-casting and photolithography of the masking layer. Oxygen reactive ion etching (100 mTorr, 20 sccm, O_2, 150 W, 20–30 min) of multiple polymer layers (epoxy-epoxy-PMMA). Spin-casting photocurable epoxy to form a masking layer and opening only on WE surface by photolithography for a hydrothermal process (3 h at 75 °C of reaction nutrient solution) for ZnO NRs growth with reaction nutrient solution composing of a 1:1 ratio of zinc nitrate hexahydrate and HMTA. Removing masking layer with acetone thoroughly and bake grown ZnO NRs (15 min

at 150 °C on a hotplate). Performing ultrasonication (1 min) to remove residues (Figure S12, Supporting Information). Dissolving the PMMA by immersion in acetone to allow release with water-soluble tape. Deposition of Ti/SiO_2 (50 nm/200 nm in thickness) by RF sputtering at the back side of the water-soluble tape as a bonding layer for subsequent integration with the substrate of the MDD DA-sensing probe.

Fabrication of Bottom Component (Ce) of the MDD DA-Sensing Probe: Processes similar to those described in the previous section except for deposition and patterning thin layers of metal (Ti/Pt; 20 nm/100 nm in thickness) used for the counter electrode in which deposited by electron beam evaporation and patterned by lift-off-techniques without any additional layers or materials (Figure S13, Supporting Information).

Fabrication Process for Double-Sided Form of DA-Sensing Probe: Oxygen plasma-treatment treatment (100 W/20 mtorr/32 s/22 sccm O_2 in O_2 plasma system, Femto Science, Korea) allows the activation on the surfaces of the substrate, as prepared in the previous section, on both sides, followed by aligning and bonding the prepared top component (WE/RE) and bottom component (CE) on each side of the substrate (Figure S14, Supporting Information). After integrating two components with the substrate, heating (70 °C for 30 min) allows strong bonding between the bonding layers (Ti/SiO_2; 50 nm/200 nm in thickness) and the substrate. Dissolving the tape by immersing it in DI water was the end of the fabrication process of the double-sided form of the DA-sensing probe (Figure S15, Supporting Information), followed by printing Ag/AgCl paste onto the RE and drying the Ag/AgCl paste in the oven (70 °C for 2 h).

Preparation of Amine-Functionalized ZnO NRs Process: The TEOS mixture was prepared by mixing ethanol (30 ml), DI (2.5 ml), aqueous ammonia (1.5 ml), and TEOS (0.1 ml). Dipping MDD DA-sensing probe tip into prepared TEOS mixture achieved silanization (—Si—$(OH)_2$) of ZnO NRs (2 h under stirring condition at room temperature). After the salinization process, washing the tip of the MDD DA-sensing probe with ethanol thoroughly several times, followed by drying the remaining liquid on the MDD DA-sensing probe at 60 °C in an oven, removed the residues of silane. Adding APTES (40 µL) into previously prepared TEOS mixture developed APTES mixture for amine-functionalization on WE surface of MDD DA-sensing probe. Dipping the tip of the MDD DA-sensing probe into the prepared APTES mixture (4 h under stirring condition at room temperature) functionalized the silanized-ZnO NRs with amine group (—NH_2). After the amine-functionalization process, cleaning the tip of the MDD DA-sensing probe by an ultrasonic bath with DI water and ethanol, followed by drying the remaining liquid on the MDD-DA sensing probe, removed residues from the reaction (Figures S16 and S17, Supporting Information).

Enzyme Immobilization Process: For the promising enzyme immobilization onto the ZnO—NH_2 NRS, dipping the tip of the MDD DA-sensing probe (3 h under stirring condition at room temperature) into the GA solution (2.5% in 0.1 M PPB, pH 5.8) as a crosslinking reagent. After crosslinking process, washing the tip of the MDD DA-sensing probe, followed by dipping the tip of the MDD DA-sensing probe into the enzyme (Tyrosinase) solution (5 mg ml^{-1} of tyrosinase in 0.05 M PBS) for overnight at 4 °C. After the enzyme immobilization process, thoroughly wash the unlinked enzyme away with DI water.

In Vitro and In Vivo Electrochemical Measurement: In vitro characterization was performed in a PBS solution (0.05 M, pH 7.4) to evaluate and optimize the performance of the MDD DA-sensing probe. The in vitro and in vivo electrochemical measurements were obtained by a potentiostat (Interface 1010E, Gamry Instruments, USA). The CV was performed between the potential of −0.5 and 0.5 V at a scan rate of 150 mV s^{-1}, and the amperometric response was performed at a potential of −350 mV versus Ag/AgCl. The longevity test of the MDD DA-sensing probe was examined by immersing it in a beaker with 0.05 M PBS solution (10 mL) by injecting 10 µl of dopamine hydrochloride (10 mM, Sigma–Aldrich, USA). Reagents used for the selectivity test such as ascorbic acid, norepinephrine, and levodopa were purchased at Sigma–Aldrich, USA.

Finite Element Analysis of Soft Mechanics of MDD DA-Sensing Probe: 3D solid mechanics and layered shell modules were used to predict the stress distribution of the MDD DA-sensing probe for various deformation modes. The device consisted of three components: top component (SU8/Cr/Au/SU8; in thickness 5 µm/7 nm/200 nm/5 µm); bottom component (SU8/Ti/Pt/SU8; in thickness 5 µm/7 nm/50 nm/5 µm); and substrate (PDMS 250 µm). The other components (enzyme, ZnO, Ti/SiO_2, and Ag/AgCl) were ignored in the simulation since they had negligible effect on the stress. The simulation of the PDMS substrate exploited the hyper elastic model (Money–Rivlin model; C10 = 0.6 MPa; C01 = 0.046 MPa). The stress of the MDD DA-sensing probe was analyzed by applying torque and force suitable for each mode. The material parameters are listed in Table S3 (Supporting Information).

In Vitro Biocompatibility Test: To validate biocompatibility of the encapsulating MDD DA-sensing probe materials, SH-SY5Y neuroblastoma cells were used for live/dead cell assay. SH-SY5Y cells were supplemented with Dulbecco's Modified Eagle's Medium (DMEM) containing 10% fetal bovine serum (FBS) and 1% penicillin/streptomycin. SH-SY5Y cells were plated at a population of 10^5 cells ml^{-1} in a petri dish (D7804-500EA, Nunc, USA) with a DA-sensing probe fixed to the bottom and incubated at 37 °C under a humidified 5% CO_2 atmosphere (Figure S18, Supporting Information). After incubation for a predetermined time (3 days), the medium was removed, and the MDD DA-sensing probe was washed in Dulbecco's phosphate buffered saline (DPBS). Live and dead SH-SY5Y cells were stained by incubating in assay reagents (calcian AM for labeling live cells and ethidium homodimer-1 for labeling dead cells) containing DPBS for 30 min. The live and dead cell images were taken by a confocal microscope (LSM 700, ZEISS, Germany).

In Vivo Biocompatibility Test: To confirm the biocompatibility in vivo, the probes in the dorsal striatum of the mouse were implanted at the following coordinates: A/P = +1.0; M/L = −1.5; D/V = −2.75. After 3 weeks of recovery, mice were anesthetized with tribromoethanol solution delivered by intraperitoneal injection (250 mg kg^{-1}), and perfused with PBS (pH 7.4) followed by 4% paraformaldehyde (PFA). To examine an inflammatory response after probe implantation, immunohistological analysis for glial cell markers was performed. Sliced brain tissues were preincubated with blocking buffer (2% normal goat serum, 0.2% bovine serum albumin, 0.3% Triton-X 100 in PBS) for 1 h at RT, and transferred to a primary antibody solution (Anti-Iba1 (Wako, 019-19741), anti-Gfap (Abcam, ab4674) diluted in the blocking buffer) for 24 h at 4 °C. And tissues were washed with washing buffer (0.2% Triton-X 100 in PBS) 15 min, three times. After washing, the brain sections were incubated in a secondary antibody solution containing DRAQ5 (ThermoFisher, 62254), Goat anti-Rabbit IgG (H+L) conjugated with Alexa Fluor 488 plus (ThermoFisher, A-48282), and Goat anti-Chicken IgG (H+L) conjugated with Alexa Fluor 568 (ThermoFisher, A-11041), for 3 h at RT. And tissues were washed with the washing buffer for 15 min, two times, and PBS for 15 min, one time. Tissues were mounted on a glass slide, and confocal imaging was performed.

Animals: Adult Sprague–Dawley male rats, 250–350 g (Samtako, South Korea), and adult C57BL/6J mice, 25–35 g (DBL, South Korea), were used for in vivo experiments. The animals were housed in groups of 2–3 rats per cage and 3–5 mice per cage under a 12 h light/dark cycle with free access to food and water ad libitum. All in vivo experiments were approved and conducted following the guidelines of the Institutional Animal Care and Use Committee at Daegu Gyeongbuk Institute of Science and Technology (DGIST-IACUC-21081101-0002).

Electrical Stimulation in MFB: For in vivo validation of the MDD DA-sensing probe, enhancement of dopamine levels in the striatum by MFB stimulation was induced. To prevent collision of the two stereotaxic arms, the stimulation electrode (NeuroNexus, MI, USA) was inserted at the left MFB with an angle of 20° posteriorly at the following coordinates: A/P = −4.4; M/L = −1.2; D/V = −7.8. The electrical stimulation consisted of biphasic pulses (2 ms per pulse) with an amplitude of 200 µA and a frequency of 60 Hz.[55,56]

In Vivo Dopamine Sensing Under Electrical Stimulation: To measure dopamine change using DA-sensing probes in vivo, normal rats were used. The rats were anaesthetized with 1–2% isoflurane and placed in a stereotaxic instrument frame. The DA-sensing probe was tested in vivo through an electrical experiment. MDD DA-sensing probe was inserted in the left stratum at the following coordinates (from bregma): anterior-posterior (A/P) = 1.3; medio-lateral (M/L) = −2.5; dorso-ventral (D/V) = −4.5. For inducing dopamine release, a stimulation electrode (NeuroNexus, MI,

USA) was inserted in the medial forebrain bundle (MFB). To prevent collision of the two stereotaxic arms, the electrode was inserted at the left MFB with an angle of 20° posteriorly at the following coordinates: A/P = −4.4; M/L = −1.2; D/V = −7.8. The electrical stimulation consisted of biphasic pulses (2 ms per pulse) with an amplitude of 200 μA and a frequency of 60 Hz. All experiments were approved and conducted following the guidelines of the Institutional Animal Care and Use committee at Daegu Gyeongbuk Institute of Science and technology (DGIST-IACUC-21081101-0002).

Unilateral Parkinson's Model Generation and Its Validation: To measure dopamine changes in a pathological condition, a unilateral Parkinson's mice model was generated using 6-OHDA toxin. Thirty minutes before 6-OHDA infusion, the mice were intraperitoneally injected with pargyline hydrochloride (5 mg kg^{-1}) and desipramine hydrochloride (25 mg kg^{-1}) solution. The mice were anesthetized with isoflurane and mounted on a stereotaxic frame. 6-OHDA (Sigma–Aldrich, H-116) solution was delivered into MFB at the following coordinates: A/P = −1.20; M/L = ±1.10; D/V = −5.00. After the surgery, post-operative care was performed on each mouse. Ibuprofen was administrated orally in drinking water for 7 days, and 5% glucose–saline was injected subcutaneously for rehydration and nutrition for 14 days. After 2 weeks of surgery, mice locomotion was recorded on Phenotyper (Noldus). The basal condition was recorded in 10 min, and apomorphine (Tocris, #2073) was subcutaneously injected and recorded in 10 min. Ethovision XT (Noldus) software was used for behavioral analysis. Nose and body point tracking data was used for rotation direction and numerical calculation. All behavioral tests were performed, and the mice were perfused for immunohistochemistry. In this immunohistochemistry experiment, anti-TH (Abcam, ab76442) and anti-DAT (Millipore, MAB369) were used on primary antibodies, and goat anti-Chicken Alexa 488 (ThermoFisher, A-11039), goat anti-Rat Alexa 568 (ThermoFisher, A-11077) were used on secondary antibodies, and DRAQ5 was used for nuclear staining.

In Vivo Dopamine Sensing in Parkinson's Mice Model: Unilateral Parkinson's model mice were anaesthetized with isoflurane and fixed on a stereotaxic frame. The DA-sensing probe was implanted on the dorsal striatum and started probe pre-conditioning for 30 min. After the pre-conditioning, the recording was started. During the current recording, L-DOPA (10 mg kg^{-1}) was intraperitoneally injected into the anaesthetized mice (Figure S19, Supporting Information).

Supporting Information

Supporting Information is available from the Wiley Online Library or from the author.

Acknowledgements

This work was supported by the National Research Foundation of Korea (NRF) funded by Ministry of Science and ICT (RS-2020-KD000093, CPS21101-130, HR22C183201, NRF-2019M3C1B8090845, NRF-2017M3A9G8084463, MOTIE 20006400, 23-SENS-01, 23-BR-04-04, RS-2023-00234581, 2020R1C1C101303014). The acknowledgements was updated to include an additional NRF grant number after initial online publication.

Conflict of Interest

The authors declare no conflict of interest.

Author Contributions

H.H.J., J.H., and J.P. contributed equally to this work. H.H.J., J.H., J.P., Y.-S.O. and K.-I.J. designed the project and wrote manuscript; H.H.J.,, J.P., S.K., J.K., H.N.J., S.K., J.Y., H.L., S.O., J.J., S.S., J.S., T.S.Y., Y.L., J.W., K.S.L., J.-C.R., J.-W.C., Y.-S.O., and K.-I.J. carried out experiments and analyzed the experimental data; J.H. led the fluid and solid mechanics modeling; and Y.-S.O. and K.-I.J. supervised the project. All of the co-authors contributed to the analysis of experimental results. The diagrams, including the mouse model (Figure 4b,h), were created with BioRender.com.

Data Availability Statement

The data that support the findings of this study are available from the corresponding author upon reasonable request.

Keywords

dopamine, electrochemical biosensors, neural probes, Parkinson's disease, soft mechanics

Received: September 20, 2023
Published online: October 20, 2023

[1] Y. Hou, X. Dan, M. Babbar, Y. Wei, S. G. Hasselbalch, D. L. Croteau, V. A. Bohr, *Nat. Rev. Neurol.* **2019**, *15*, 565.
[2] C. B. Vaughn, D. Jakimovski, K. S. Kavak, M. Ramanathan, R. H. B. Benedict, R. Zivadinov, B. Weinstock-Guttman, *Nat. Rev. Neurol.* **2019**, *15*, 329.
[3] M. Quintero Escobar, J. G. D. M. Pontes, L. Tasic, *Brain Res.* **2021**, *1773*, 147704.
[4] W. Poewe, K. Seppi, C. M. Tanner, G. M. Halliday, P. Brundin, J. Volkmann, A.-E. Schrag, A. E. Lang, *Nat. Rev. Dis. Primers* **2017**, *3*, 17013.
[5] J. D. Berke, *Nat. Neurosci.* **2018**, *21*, 787.
[6] J. C. Felger, M. T. Treadway, *Neuropsychopharmacology* **2017**, *42*, 216.
[7] G. Lunardi, S. Galati, D. Tropepi, V. Moschella, L. Brusa, M. Pierantozzi, A. Stefani, S. Rossi, F. Fornai, E. Fedele, P. Stanzione, A. H. Hainsworth, A. Pisani, *Parkinsonism Relat. Disord.* **2019**, *15*, 383.
[8] J. D. Berke, S. E. Hyman, *Neuron* **2000**, *25*, 515.
[9] A. E. Kelley, K. C. Berridge, *J. Neurosci.* **2002**, *22*, 3306.
[10] H. Gu, E. L. Varner, S. R. Groskreutz, A. C. Michael, S. G. Weber, *Anal. Chem.* **2015**, *87*, 6088.
[11] S. Kang, J. Park, Y. Jeong, Y.-S. Oh, J.-W. Choi, *Anal. Chem.* **2022**, *94*, 11459.
[12] A. Jaquins-Gerstl, A. C. Michael, *Analyst* **2015**, *140*, 3696.
[13] A. Prasad, Q.-S. Xue, V. Sankar, T. Nishida, G. Shaw, W. J. Streit, J. C. Sanchez, *J. Neural Eng.* **2012**, *9*, 056015.
[14] F. Wu, E. Stark, P.-C. Ku, K. D. Wise, G. Buzsáki, E. Yoon, *Neuron* **2015**, *88*, 1136.
[15] H. Shin, Y. Son, U. Chae, J. Kim, N. Choi, H. J. Lee, J. Woo, Y. Cho, S. H. Yang, C. J. Lee, I.-J. Cho, *Nat. Commun.* **2019**, *10*, 3777.
[16] D. M. D. Landis, *Annu. Rev. Neurosci.* **1994**, *17*, 133.
[17] S. Schmidt, K. Horch, R. Normann, *J Biomed Mater Res* **1993**, *27*, 1393.
[18] D. H. Szarowski, M. D. Andersen, S. Retterer, A. J. Spence, M. Isaacson, H. G. Craighead, J. N. Turner, W. Shain, *Brain Res.* **2003**, *983*, 23.
[19] R. J. J. Van Daal, J.-J. Sun, F. Ceyssens, F. Michon, M. Kraft, R. Puers, F. Kloosterman, *J Neural Eng* **2020**, *17*, 016046.
[20] A. Mercanzini, K. Cheung, D. L. Buhl, M. Boers, A. Maillard, P. Colin, J.-C. Bensadoun, A. Bertsch, P. Renaud, *Sens Actuators A Phys* **2008**, *143*, 90.
[21] J.-W. Jeong, J. G. Mccall, G. Shin, Y. Zhang, R. Al-Hasani, M. Kim, S. Li, J. Y. Sim, K.-I. Jang, Y. Shi, D. Y. Hong, Y. Liu, G. P. Schmitz, L. Xia,

Z. He, P. Gamble, W. Z. Ray, Y. Huang, M. R. Bruchas, J. A. Rogers, *Cell* **2015**, *162*, 662.
[22] I. R. Minev, P. Musienko, A. Hirsch, Q. Barraud, N. Wenger, E. M. Moraud, J. Gandar, M. Capogrosso, T. Milekovic, L. Asboth, R. F. Torres, N. Vachicouras, Q. Liu, N. Pavlova, S. Duis, A. Larmagnac, J. Vörös, S. Micera, Z. Suo, G. Courtine, S. P. Lacour, *Science* **2015**, *347*, 159.
[23] K. C. Cheung, P. Renaud, H. Tanila, K. Djupsund, *Biosens. Bioelectron.* **2007**, *22*, 1783.
[24] Y.-Y. Chen, H.-Y. Lai, S.-H. Lin, C.-W. Cho, W.-H. Chao, C.-H. Liao, S. Tsang, Y.-F. Chen, S.-Y. Lin, *J Neurosci Methods* **2009**, *182*, 6.
[25] S. P. Lacour, S. Benmerah, E. Tarte, J. Fitzgerald, J. Serra, S. Mcmahon, J. Fawcett, O. Graudejus, Z. Yu, B. Morrison III, *Med. Biol. Eng. Comput.* **2010**, *48*, 945.
[26] S. Wurth, M. Capogrosso, S. Raspopovic, J. Gandar, G. Federici, N. Kinany, A. Cutrone, A. Piersigilli, N. Pavlova, R. Guiet, G. Taverni, J. Rigosa, P. Shkorbatova, X. Navarro, Q. Barraud, G. Courtine, S. Micera, *Biomaterials* **2017**, *122*, 114.
[27] J. Rivnay, H. Wang, L. Fenno, K. Deisseroth, G. G. Malliaras, *Sci. Adv.* **2017**, *3*, e1601649.
[28] J. G. Roberts, L. Z. Lugo-Morales, P. L. Loziuk, L. A. Sombers, *Methods Mol Biol* **2013**, *964*, 275.
[29] H. L. Rowley, K. F. Martin, C. A. Marsden, *J Neurosci Methods* **1995**, *57*, 93.
[30] K. N. Hascup, E. R. Hascup, *Comp. Med.* **2014**, *64*, 249.
[31] Y. Guo, S. Jiang, B. J. B. Grena, I. F. Kimbrough, E. G. Thompson, Y. Fink, H. Sontheimer, T. Yoshinobu, X. Jia, *ACS Nano* **2017**, *11*, 6574.
[32] A. J. Bard, L. R. Faulkner, H. S. White, *Electrochemical Methods: Fundamentals and Applications*, 3rd ed., Wiley, New York **2022**.
[33] D. A. Skoog, F. J. Holler, T. A. Nieman, *Principles of Instrumental Analysis*, Saunders College Publishing, Orlando, FL **1998**.
[34] G. Jerkiewicz, *ACS Catal.* **2022**, *12*, 2661.
[35] L. Ribovski, F. A. Dos Santos, V. Zucolotto, B. C. Janegitz, *J. Solid State Electrochem.* **2019**, *23*, 1581.
[36] S. L. Chia, D. T. Leong, *Heliyon* **2016**, *2*, e00177.
[37] A. Costantini, V. Califano, *Catalysts* **2021**, *11*, 629.
[38] C.-S. Yang, R. A. Bley, S. M. Kauzlarich, H. W. H. Lee, G. R. Delgado, *J. Am. Chem. Soc.* **1999**, *121*, 5191.
[39] M. A. Karakassides, D. Gournis, D. Petridis, *Clay Miner.* **1999**, *34*, 429.
[40] S. L. Chia, D. T. Leong, *Heliyon* **2016**, *2*, e00177.
[41] K. S. Aneja, S. Bohm, A. S. Khanna, H. L. M. Bohm, *Nanoscale* **2015**, *7*, 17879.
[42] L. Wang, Y. Ye, X. Lu, Z. Wen, Z. Li, H. Hou, Y. Song, *Sci. Rep.* **2013**, *3*, 3568.
[43] J. Li, J. Gao, T. Guo, X. Huang, X. Zhang, C. Xu, H. Xue, *ACS Appl Polym Mater* **2019**, *1*, 3148.
[44] M. Caglar, S. Ilican, Y. Caglar, F. Yakuphanoglu, *Appl. Surf. Sci.* **2009**, *255*, 4491.
[45] M. M. Pérez-Madrigal, F. Estrany, E. Armelin, D. D. Díaz, C. Alemán, *J. Mater. Chem. A* **2016**, *4*, 1792.
[46] B. Molina, E. Domínguez, E. Armelin, C. Alemán, *Gels* **2018**, *4*, 86.
[47] G. Ruano, B. G. Molina, J. Torras, C. Alemán, *Molecules* **2021**, *26*, 4345.
[48] H. Xicoy, B. Wieringa, G. J. M. Martens, *Mol Neurodegener* **2017**, *12*, 10.
[49] S. G. Pantelakis, C. A. Rodopoulos, *Engineering Against Fracture: Proceedings 339 of the 1st Conference*, Springer, Berlin, Germany **2009**.
[50] K. Abbas, S. Alaie, M. Ghasemi Baboly, M. M. M. Elahi, D. H. Anjum, S. Chaieb, Z. C. Leseman, *J. Micromech. Microeng.* **2016**, *26*, 015007.
[51] E. J. Kappert, M. J. T. Raaijmakers, K. Tempelman, F. P. Cuperus, W. Ogieglo, N. E. Benes, *J. Membr. Sci.* **2019**, *569*, 177.
[52] R. D. Jaeger, M. Gleria, *Inorganic Polymers*, Nova Science Publishers, New York, **2007**.
[53] A. Bonaccini Calia, E. Masvidal-Codina, T. M. Smith, N. Schäfer, D. Rathore, E. Rodríguez-Lucas, X. Illa, J. M. De La Cruz, E. Del Corro, E. Prats-Alfonso, D. Viana, J. Bousquet, C. Hébert, J. Martínez-Aguilar, J. R. Sperling, M. Drummond, A. Halder, A. Dodd, K. Barr, S. Savage, J. Fornell, J. Sort, C. Guger, R. Villa, K. Kostarelos, R. C. Wykes, A. Guimerà-Brunet, J. A. Garrido, *Nat. Nanotechnol.* **2022**, *17*, 301.
[54] S. L. Thiele, R. Warre, J. E. Nash, *J Vis Exp* **2012**, *60*, e3234.
[55] H. N. Schwerdt, M. J. Kim, S. Amemori, D. Homma, T. Yoshida, H. Shimazu, H. Yerramreddy, E. Karasan, R. Langer, A. M. Graybiel, M. J. Cima, *Lab Chip* **2017**, *17*, 1104.
[56] M. K. Zachek, P. Takmakov, J. Park, R. M. Wightman, G. S. Mccarty, *Biosens. Bioelectron.* **2010**, *25*, 1179.